

Refined DFT recipe and renormalisation of band-edge parameters for electrons in monolayer MoS₂ informed by the measured spin-orbit splitting

Igor Rozhansky,¹ Michele Masseroni,² Ricardo Pisoni,² Suad Alshammary,^{1,3}
Xue Li,¹ Thomas Ihn,² Klaus Ensslin,² James McHugh,¹ and Vladimir Fal'ko¹

¹*National Graphene Institute, University of Manchester, Manchester M13 9PL, United Kingdom*

²*Laboratory for Solid State Physics, ETH Zürich, CH-8093 Zürich, Switzerland*

³*Physics Department, Faculty of science, Northern Border University, Arar, Saudi Arabia*

Conduction band-edge spin-orbit splitting (SOS) in monolayer transition metal dichalcogenides determines a competition between bright and dark excitons and sets conditions for spintronics applications of these semiconductors. Here, we report the SOS measurement for electrons in monolayer MoS₂, found from the threshold density, n_* , for the upper spin-orbit-split band population, which exceeds by an order of magnitude the values expected from the conventional density functional theory (DFT). Theoretically, half of the observed value can be attributed to the exchange enhancement of SOS in a finite-density electron gas, but explaining the rest requires refining the DFT approach. As the conduction band SOS in MoS₂ is set by a delicate balance between the contribution of sulphur p_x and p_y orbitals and $d_{z^2} - d_{xz}$ and $d_{z^2} - d_{yz}$ mixing in molybdenum, we use a DFT+U+V framework for fine-tuning the orbital composition of the relevant band-edge states. An optimised choice of Hubbard U/V parameters produces close agreement with the experimentally observed conduction band SOS in MoS₂, simultaneously resulting in the valence-band SOS and the quasi-particle band gap which are closer to their values established in the earlier-published experiments.

I. INTRODUCTION

Transition metal dichalcogenides (TMDs) are a promising group of two-dimensional semiconductors for a wide range of electronics [1–3], optoelectronics [4, 5] and spintronics [6–9] device applications [8–14]. Among those, monolayer molybdenum disulphide (MoS₂) stands out because of its environmental stability, efficient electrostatic doping with the already-demonstrated high electron mobility, and the prospects of wafer-scale growth [15–21]. For that reason, an efficient modelling tool for the properties of charge carriers in MoS₂ is highly desirable, including both microscopic insight into their single-particle characteristics based on density functional theory (DFT) and mesoscale many-body analysis of electron-electron correlation effects. Although a massive volume of DFT coding has already been developed and realized in several 2D materials databases and reviews [22–29], a satisfactory fine-energy-scale agreement between the DFT-computed and experimentally-measured spin-orbit splitting (SOS) has yet to be achieved for monolayer MoS₂ conduction band (CB) electrons: its DFT-computed values are negligibly small (only a few meV) [30–33] as compared to the marks set by various experiments (≥ 10 meV) [34–38].

The purpose of the present study is to perform a detailed comparison of the experimentally-measured characteristics of spin-orbit-split electron bands in monolayer MoS₂ (Fig. 1b) with the results of multi-scale modelling of those characteristics: the CB SOS, Δ , and effective masses at the K-point band edges of MoS₂ Brillouin zone. Experimentally, as described in Section II these characteristics are determined by analysing the measured Shubnikov de Haas oscillations (SdHO, Fig. 1a), enabling us to find the band mass of electrons and determine the

threshold doping density, n_* , at which electrons filling reaches the bottom of the higher spin-orbit-split band, identified using the SdHO Fourier spectrum in Fig. 1c.

The multi-scale modelling part of this work incorporates two components. First, in Section III we analyse many-body enhancement of a single-particle SOS, Δ_0 : it has recently been shown that 'bare' SOS is enhanced by exchange interaction between electrons in 2D semiconductors [39, 40], leading to the density dependence culminating at the threshold density, n_* . To mention, the threshold density n_* is important for spintronics based on MoS₂-based FETs, as it separates the regimes of slow and fast spin and valley relaxation of charge carriers [39, 41]. This enables us to determine Δ_0 in monolayer MoS₂ from the experimentally measured n_* value and, then, to compare it with the DFT results. Based on that comparison, in Section IV, we propose an extension of the commonly-used DFT approach to include both on-site (U) and inter-site (V - between metal and chalcogen) Hubbard terms within DFT+U+V in order to reproduce the extracted bare SOS value, simultaneously complying with the valence band SOS and the quasi-particle band gap, E_g .

II. MAGNETOTRANSPORT DATA AND SdHO ANALYSIS

The reported experiments were conducted on a dual-gated multi-terminal MoS₂ device. The sample consists of a monolayer MoS₂ - encapsulated in hexagonal boron nitride (hBN), with pre-patterned metallic bottom contacts and graphite top and bottom gates. This sample is the same as the one presented in Ref. [35], and its fabrication details are provided in the Supplemental Information [42]. The measured four-terminal resistance, R_{xx} is shown in Fig. 1a as a function of the bottom gate voltage,

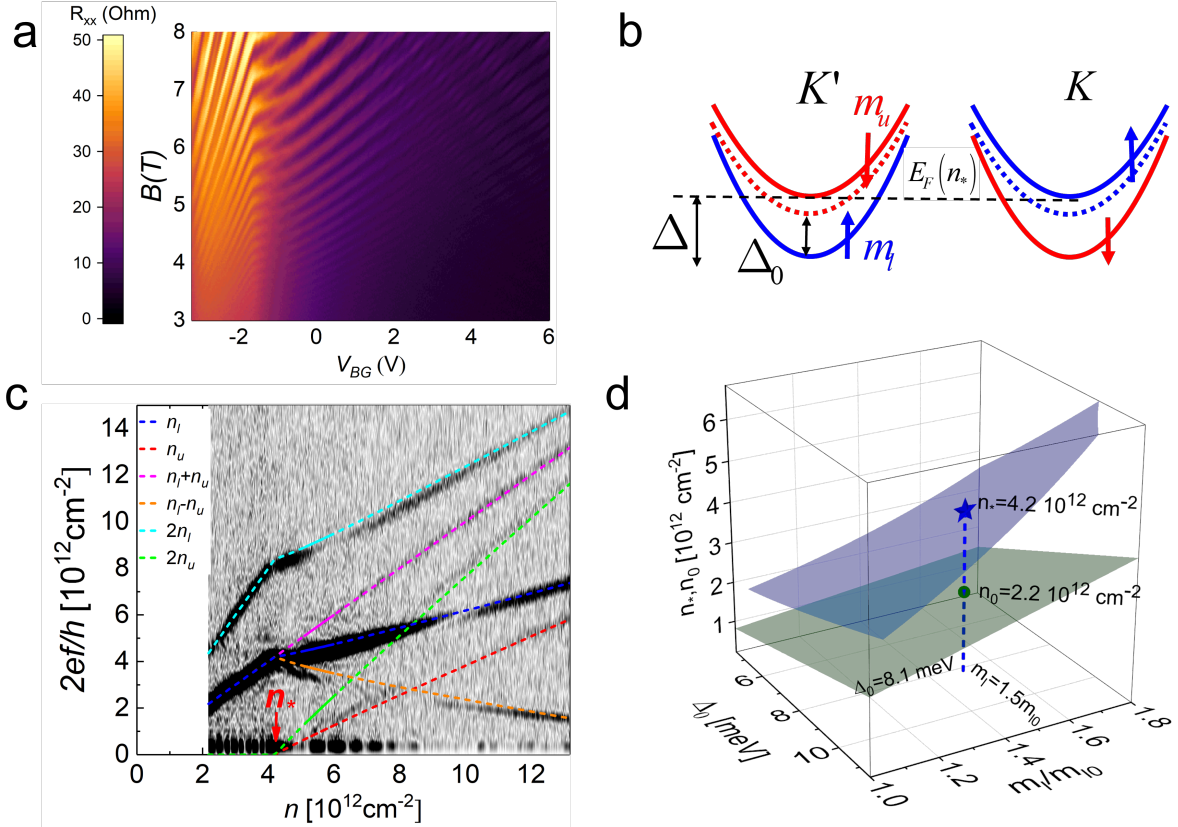


FIG. 1. Comparison of experimental data and theoretical predictions for spin-split band fillings. (a) Four-terminal resistance R_{xx} as a function of the bottom gate voltage V_{BG} and magnetic field B . (b) Band diagram indicating SOS conduction band of MoS₂ monolayer, effective masses m_u and m_l (red: spin down, blue: spin up) at the $\pm K$ valleys. The bare SOS Δ_0 (dotted) increases to Δ (solid) by exchange interaction. The dashed horizontal line marks the Fermi level E_F at the upper band filling threshold density, n_* . (c) Density, n , dependence of the Fourier spectrum of Shubnikov-de Haas oscillations with the frequency $f * 2e/h$ rescaled to represent electron sheet densities in the lower (n_l) and upper (n_u) spin-split bands, along with their combinations. The threshold density $n_* = 4.2 \times 10^{12} \text{ cm}^{-2}$ marks onset of populating the upper spin-split band. At high-density end, n_l and n_u change almost linearly with n ; from their slopes we estimate $m_u/m_l \approx 1.3$ as the ratio between the upper and lower spin-split band masses. One may notice deviations from linear behaviour of n_u near n_* , which is attributed to the electron-electron interaction as discussed in the Supplemental Information [42] and with the calculated results shown by dashed lines. (d) The threshold density n_* (blue surface) calculated from Eq. (2) as a function of the lower band effective mass m_l (normalised by the DFT-computed value $m_{l0} \approx 0.43m_e$) and bare SOS, Δ_0 , in comparison to threshold density n_0 evaluated without exchange renormalisation of SOS (green surface).

V_{BG} , and the perpendicular magnetic field, B . For this measurement, the top-gate voltage was set to $V_{TG} = 8$ V to ensure ohmic contact behaviour. The observed resistance exhibits clear SdHO that can be precisely described at low densities in terms of a single band of electrons with simple Kramers degeneracy. As reported earlier [35], temperature dependence of the amplitudes of these low-density SdHO is fitted well by effective mass $m_l = 0.65m_e$, attributed to the lower spin-split subband electrons, which is about 1.5 times bigger than typical values, $m_{l0} \approx 0.43m_e$, obtained in DFT calculations [29–33]. Note that this value is consistent with other published experimental data [43].

At the higher densities, corresponding to the gate voltage $V_{BG} > V_*$, the SdHO pattern acquires a pronounced beating pattern and the SdHO fan plot changes its gra-

dients (a ‘kink’), indicating that, at $V_{BG} > V_*$, the total electron density is shared by two spin-split bands [35]. As a result, from the value of V_* in Fig. 1a we determine the critical value, $n_* = 4.2 \times 10^{12} \text{ cm}^{-2}$, of the electron sheet density at which the Fermi level in MoS₂ reaches the bottom of its upper spin-split band. The onset of the upper spin-split band occupation by electrons is even more obvious in the Fourier Transform of the $R_{xx}(B^{-1})$ data (performed for each V_{BG} with the Fourier frequency rescaled into ‘density units’, as $2ef/h$), then plotted as a function of the total gate-controlled density, n , in Fig. 1c. Note that this Fourier spectrum enables us to determine the carrier densities in both lower, n_l , and upper, n_u , spin-split bands, traced with blue and red dashed lines, respectively, and the identified density value, n_* , determined from Fig. 1c raises an immediate issue, as the esti-

mate for the upper spin-split band occupancy threshold using $\Delta_0 \approx 3$ meV and $m_{l0} \approx 0.43m_e$, as typically computed by DFT for undoped material, gives a threshold density $\Delta_0 m_{l0} / \pi \hbar^2 \approx 5 \times 10^{11} \text{ cm}^{-2}$, which is about an order of magnitude below the experimentally measured value.

III. RENORMALIZATION OF BARE BAND PARAMETERS BY ELECTRON-ELECTRON INTERACTION

A meaningful comparison between DFT-based band parameters and the experimentally determined threshold n_* requires accounting for correlation-induced effects changing both SOS and the band mass [39, 40, 44–47], in particular, since the Wigner-Seitz radius is large throughout the density range covered by the data set in Fig. 1c, up to n_* . On the one hand, as the experimental data in Section II offer the actual - that is, renormalised - band edge mass, we approximate the dispersion of the lower spin-split conduction band as parabolic, with the experimentally determined mass $m_l \approx 0.65m_e$, which sets the relation between doping density and the Fermi energy of electrons. The validity of the parabolic approximation is supported by the nearly constant SdHO period while filling the lower band. On the other hand, we fully account for the many-body renormalisation of SOS and use it to determine the values of bare SOS, Δ_0 , from the experimentally identified threshold density, $n_* = 4.2 \times 10^{12} \text{ cm}^{-2}$. To mention, that part of the calculation is based on the use of a bare band-edge mass, $m_{l0} \approx 0.43m_e$, consistently found in various DFT calculations [29–33].

To realise the above-described strategy, we analyse the screened-exchange electron self-energy,

$$\Sigma(\mathbf{k}, \omega) = - \int \frac{d^2 q d\Omega}{(2\pi)^3} \frac{V(q) G(\mathbf{k} - \mathbf{q}, \omega - \Omega)}{1 + V(q) \Pi(q, \Omega)}; \\ V(q) = \frac{2\pi e^2 / \varepsilon}{q(1 + r_* q)}; \quad r_* = \frac{\epsilon_{\parallel} - \epsilon_{\perp}^{-1} \varepsilon^2}{2\varepsilon} d. \quad (1)$$

Here, we implement 2D dielectric screening via the Keldysh potential (with screening length [48, 49], r_* , dependent on the film thickness, d) and metallic screening; $G(\mathbf{k}, \omega) = [\omega - (\hbar^2 k^2 / 2m_{l0} - E_F)]^{-1}$ is the free valley-polarised electron Green's function in the lower SOS band; $\Pi(\mathbf{q}, \Omega)$ is the polarisation bubble describing metallic screening; and $\varepsilon = \sqrt{\varepsilon_{\parallel} \varepsilon_{\perp}}$ stands for the dielectric constant of the encapsulation environment (hBN) with in/out-of-plane dielectric constants, $\varepsilon_{\parallel}/\varepsilon_{\perp}$. We use an effective dielectric constant for the hBN-encapsulated environment of $\varepsilon = 4.6$ [50]; For the in-plane and out-of-plane dielectric constant for MoS₂ monolayer we take the values [51, 52] $\epsilon_{\parallel} = 15.46$, $\epsilon_{\perp} = 6.46$, $d = 5.48 \text{ \AA}$, resulting in $r_* \varepsilon \approx 33 \text{ \AA}$.

At the threshold density n_* , Fermi level in the occupied lower band reaches the bottom of the upper spin-split

band. Using the experimentally determined lower band mass, m_l , this condition reads as,

$$\frac{\pi \hbar^2 n_*}{m_l} = \Delta(n_*) \equiv \Delta_0 + \Sigma(0, 0). \quad (2)$$

Here, density-dependent self-energy correction is computed with statically screened interaction, implemented with $\Pi(q, 0)$ at T=0. While for non-interacting 2D electrons $\Pi(q, 0)$ is determined only by the bare mass, m_{l0} , electron-electron correlations introduce [44] density dependence of Π . Some simplification for our calculations comes from that such density dependence needs to be accounted in the long wave length limit, $\Pi(q \rightarrow 0, 0)$: while the static Lindhard function, $\Pi_0(q < 2k_F, 0) = m_{l0} / \pi \hbar^2$ is rigorously constant for all wave vectors up to $2k_F$, the divergence of $V(q)$ at $q \rightarrow 0$, indicates that screening is dominated by the small- q contributions. To describe the density dependence of $\Pi(q \rightarrow 0, 0)$, Hwang and Das Sarma [53] proposed to expand it into a power series in $r_s = \frac{m_{l0} e^2}{\varepsilon \hbar^2 \sqrt{\pi n}}$, the Wigner-Seitz radius (here, m_{l0} is used to avoid double-counting of perturbation theory diagrams), and they have explored the first term in such an expansion. Here, we replicate their approach [53], but extend such a calculation onto the second order in r_s :

$$\Pi(q \rightarrow 0, 0) \approx \frac{m_{l0}}{\pi \hbar^2} (1 + \aleph_1 r_s + \aleph_2 r_s^2), \quad (3)$$

For this, we sum a standard set [54–57] of diagrams drawn in Fig. 2a. A table inset in Fig. 2b summarises the computed values of those 1st-order (Π_1) and 2nd-order ($\Pi_2 = \Pi_2^{(1)} + \Pi_2^{(2)}$) contributions, where $\Pi_2^{(1)}$ and $\Pi_2^{(2)}$ correspond to one- and two-loop diagrams in Fig. 2a, respectively. The numerical integration of those diagrams produces $\aleph_1 = 0.29$, $\aleph_2 = -0.08$. The opposite signs of the obtained 1st and 2nd order contributions hints at an alternating-sign series. Therefore, we consider the 1st-order, Π_{\max} , and the 2nd-order, Π_{\min} , results as the respective upper and lower bounds for the actual polarisation bubble values, and use their median, $\Pi_* = (\Pi_{\max} + \Pi_{\min})/2$, to relate the threshold density n_* to Δ_0 :

$$\Pi_{\max} = \frac{m_{l0}}{\pi \hbar^2} (1 + 0.29 r_s); \\ \Pi_{\min} = \frac{m_{l0}}{\pi \hbar^2} (1 + 0.29 r_s - 0.08 r_s^2); \\ \Pi_* = \frac{m_{l0}}{\pi \hbar^2} (1 + 0.29 r_s - 0.04 r_s^2). \quad (4)$$

This procedure produces the dependence shown in Fig. 1d, where the effect of the SOS enhancement is demonstrated by comparing those values with threshold densities computed with bare SOS.

At this point, we also need to comment on that the experimentally measured mass (also used in Eq. (2)) is quite heavier than the typically DFT-computed value for MoS₂ [29–33]. The earlier studies of mass renormalization in 2D semiconductors [58] and some recent studies

[45–47, 59] suggested a substantial mass enhancement in 2D systems with $r_s \gg 1$. To estimate mass enhancement for electrons in MoS₂ at densities around n_* , where $r_s \sim 5$, we use the on-shell approximation suggested in Refs. [45–47],

$$\frac{m_{l0}}{m_l} = 1 + \frac{m_{l0}}{\hbar^2 k_F} \frac{d}{dk} \text{Re} \Sigma \left(k, \frac{\hbar^2 (k^2 - k_F^2)}{2m_{l0}} \right) \Big|_{k=k_F}.$$

For this, dynamical polarisability $\Pi(q, \omega)$ is required, which is rather difficult to evaluate within the expansion in r_s . In practice, we retain both momentum- and frequency-dependence of $\Pi_0(q, \omega)$ (see Supplemental Information [42]), but approximate the higher-order corrections by constant terms already used in the SOS renormalisation analysis. Figure 2b displays mass renormalisation estimated using $\Pi(q, \omega) = \Pi_0(q, \omega) + 0.29r_s \frac{\pi\hbar^2}{m_{l0}}$, (blue dashed line), $\Pi(q, \omega) = \Pi_0(q, \omega) + (0.29r_s - 0.08r_s^2) \frac{\pi\hbar^2}{m_{l0}}$, (red dashed line), and the median, $\Pi(q, \omega) = \Pi_0(q, \omega) + (0.29r_s - 0.04r_s^2) \frac{\pi\hbar^2}{m_{l0}}$, (solid red line). For $r_s = 5$, all these curves show mass enhancement 35%–45%, close enough to the experimentally inferred 50% enhancement.

Finally, we use the calculated SOS renormalisation with the measured n_* and m_l values in Eq. (2) and determine bare SOS value, $\Delta_0 \approx 8.1$ meV, which remains substantially larger than all the existing DFT predictions [24, 29, 31, 60, 61], despite the already incorporated exchange enhancement that reaches the maximum value at the threshold density[62]. This suggests that fine tuning of the DFT approach is needed in order to resolve the remaining discrepancy.

IV. DFT+U+V RECIPE REFINED TO REPRODUCE THE EXTRACTED BARE SOS VALUES

To identify how to tune DFT modelling to change its predictions for SOS at the K-point conduction band edge, we examine the underlying microscopic SOS mechanisms, as illustrated by a sketch in Fig. 3a. As those MoS₂ conduction band edges are dominated by molybdenum d_{z^2} orbitals [29, 63], which have zero out-of-plane angular momentum projection ($L_z = 0$), the atomic SOC of the transition metal itself does not directly produce the SOS in the band. Instead, it is composed of two contributions (see Supplemental Information [42] for details): (i) a small admixture of sulphur p_x and p_y orbitals, which carry orbital angular momentum projection $L_z = \mp 1$, brings sulphur's SOS into the conduction band dispersion, set by a spin-orbit constant, J_S ; and (ii) second-order perturbative mixing by the off-diagonal component of atomic SOC in molybdenum, J_{Mo} , between c -band's d_{z^2} orbitals and d_{xz} and d_{yz} orbitals ($L_z = \mp 1$) that dominate the $c+1$ conduction band at $\pm K$, as illustrated in

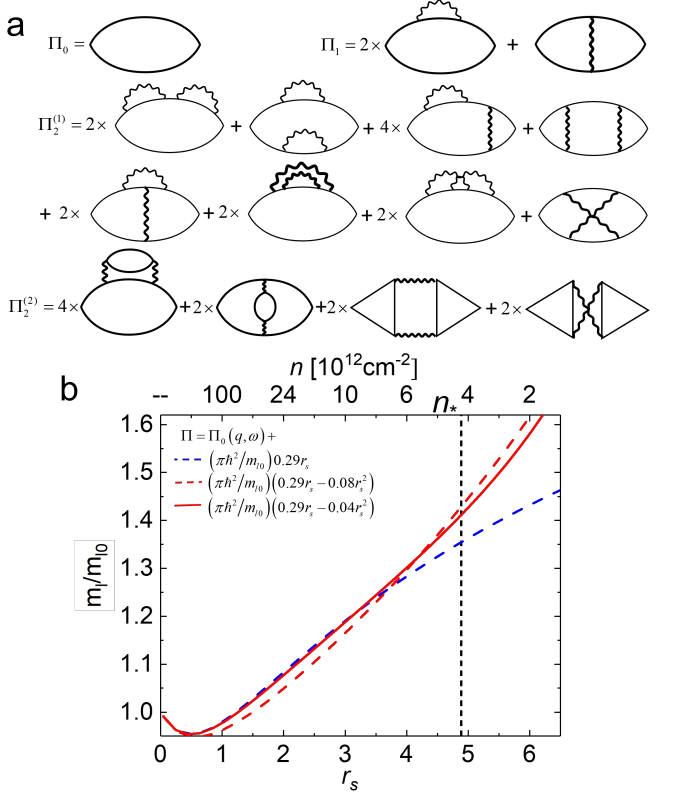


FIG. 2. (a) Set of diagrams contributing to the polarisability. (b) Calculated mass renormalisation. The dashed blue and red lines show the mass renormalisation using a static first- and second-order correction to the polarisability, respectively. Red solid line is calculated with the median $\Pi(q, \omega) = \Pi_0(q, \omega) + (0.29r_s - 0.04r_s^2) \frac{\pi\hbar^2}{m_{l0}}$; the top and bottom axis show the electron density and corresponding Wigner-Seitz radius r_s , vertical dashed line corresponds to $n_* = 4.2 \times 10^{12} \text{ cm}^{-2}$, $r_s(n_*) = 4.9$.

Fig. 3a. Together, these two mechanisms give [42],

$$\Delta_0 = J_S w_S^c - \frac{3}{2} \frac{J_{\text{Mo}}^2 w_{\text{Mo}}^c w_{\text{Mo}}^{c+1}}{E_{c+1} - E_c}, \quad (5)$$

where w_S^c (w_{Mo}^{c+1}) and E_c (E_{c+1}) are the weights and band-edge energies of the relevant p -orbitals of sulphur in the c band (Mo d_{xz} , d_{yz} -orbitals in the $c+1$ band), respectively. As atomic SOC constant $J_S > 0$, the two terms in Eq. (5) set opposite trends, suggesting that they accidentally cancel each other in the earlier implemented DFT computations producing $\Delta_0 \approx 3$ meV. As the balance of such a cancellation is sensitive to the orbital composition of c and $c+1$ bands, we argue that a very small, SOS ~ 3 meV, emerged in those DFT studies of MoS₂, arises from an underestimated Mo-S hybridisation. Furthermore, the above discussion can be extended [42] onto the SOS in the top monolayer in an electrically biased few-layer films studied in Refs [64–68], which shows that the interlayer hybridisation of orbitals, described in Supplemental Information [42], can produce a small reduction

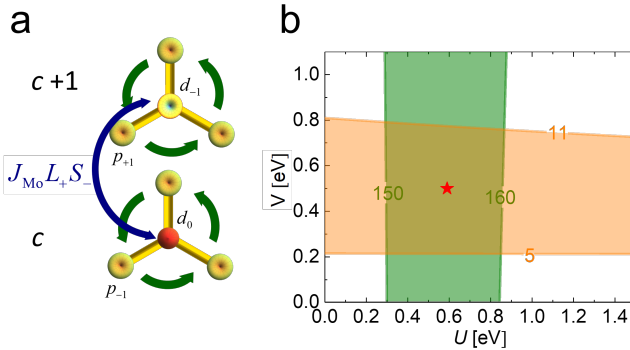


FIG. 3. (a) Sketch illustrating how SOS is generated for electrons at the K-valley conduction band edge of MoS₂ monolayer. The contributing molybdenum d and sulphur p orbitals are indicated together with their out-of-plane angular momentum projections. Green arrows represent the kinematic angular momentum κ_z arising from the Bloch phase factor. Intralayer coupling between conduction and upper conduction band (denoted as c and $c+1$, respectively) arises from the part of the atomic spin-orbit operator, $J_{\text{Mo}} L - S_+$, where J_{Mo} is the atomic spin-orbit constant of the molybdenum atom. (b) Hubbard U and V parameters yielding the range of the conduction-band SOS, Δ_0 , (orange area) and valence band SOS, Δ_v , (green area). Red star marks the optimal parameters $U_* = 0.59$ eV and $V_* = 0.5$ eV, corresponding to SOS $\Delta_0 = 8.1$ meV, $\Delta_v = 155$ meV.

in the value of the on-layer SOS.

To tune the orbital structure of the bands and promote Mo-S hybridisation towards obtaining bare SOS in the range of $\Delta_0 \sim 10$ meV, we employ the DFT+U+V approach [69], which includes the inter-site (closest neighbour) Hubbard interaction V of electrons in orbitals belonging to metal and chalcogen sites, and perform DFT+U+V calculations using the Quantum ESPRESSO code. A $31 \times 31 \times 1$ Monkhorst-Pack k -point grid is used to sample the Brillouin zone, with plane-wave and charge density cutoffs of 80 and 800 eV, respectively, and a Fermi-Dirac smearing of the electronic distribution of width $\sigma = 0.01$ eV. Optimised fully-relativistic Vanderbilt norm-conserving pseudopotentials were used to approximate electron-ion interactions and to include spin-orbit coupling in all calculations.

Figure 3b shows the computed U, V -dependence of the conduction-band SOS, Δ_0 , together with the valence-band SOS, Δ_v . The computed data are mapped onto the plane of input parameters, U and V . Here, the green-painted area identifies the range where the values of the DFT+U+V computed valence-band SOS, Δ_v , fall within the range set by the earlier published experimental studies of the MoS₂ valence band properties [37, 70–73]; the orange-painted area covers the range that yields $5 \text{ meV} < \Delta_0 < 11 \text{ meV}$, chosen to fit between the values of bare SOS extracted from the experimentally measured n_* using $\Pi_{\min} < \Pi < \Pi_{\max}$ in Eq. 4. The red star marks the optimal choice, $U_* = 0.59$ eV and $V_* = 0.5$ eV, that

gives $\Delta_0 = 8.1$ meV, as obtained from the measured n_* using the median Π_* , and $\Delta_v = 155$ meV. To mention, the computed effective conduction band masses are almost independent of U and V across the analysed range (e.g., $m_{u0} = 0.485m_e$ and $m_{l0} = 0.433m_e$ for $U_* = 0.59$ eV and $V_* = 0.5$ eV).

We also note that the implementation of DFT+U+V with $U_* = 0.59$ eV and $V_* = 0.5$ eV significantly improves the agreement between the computed band gap, which increases to $E_g = 1.90$ eV (as compared to ≈ 1.7 eV at $U = V = 0$), and the bounds [74] set by the experimentally established optical (≈ 1.80 eV) and quasiparticle (≈ 2.16 eV) monolayer band gaps [75, 76]. Overall, the obtained parameters support a picture of unconventional screening, combining weak short-range and stronger long-range Hubbard interactions [77].

V. SUMMARY

Based on the analysis of Shubnikov de Haas oscillations, observed in monolayer MoS₂, we found the threshold density, n_* , for the onset of filling the states in the upper spin-orbit split (SOS) conduction band in this material, which appeared to be much higher than the value anticipated based on the earlier DFT-computed band parameters of MoS₂. While the doping-induced (hence, doping-dependent) exchange enhancement of SOS and mass enhancement partly explain the discrepancy between DFT results and the measured density threshold, theory and experiment for the conduction-band spin-orbit splitting in monolayer MoS₂, the estimated value of bare SOS, $\Delta_0 \approx 8.1$ meV, required to obtain the measured threshold density is still much higher than the previously DFT-computed values. However, the discrepancy can be resolved by using a compact DFT+U+V computational scheme that simultaneously corrects the conduction- and valence-band SOS, while improving the prediction for the quasiparticle band gap: we argue that conventional DFT approach severely underestimates the conduction-band SOS due to an accidental cancellation of orbital contributions when correlations are neglected. Including on-site $U_* = 0.59$ eV and inter-site $V_* = 0.5$ eV Hubbard interaction provides the value of Δ_0 extracted from the experiment, as well as produces the valence-band SOS and the monolayer band gap values closer to the experimentally established ones. The resulting approach offers a computationally efficient route to accurate spin-orbit and band-edge parameters across the TMDs family without resorting to resource-hungry GW methods.

VI. ACKNOWLEDGEMENTS

We thank A. Principi, Y. Gindikin, L. Golub and M. Potemski for valuable discussions. We acknowledge support from 2DFERROPLEX project funded by

the European Union under grant agreement 101223116, EPSRC Grants EP/S019367/1, EP/P026850/1, and EP/N010345/1; British Council project 1185409051. X.L. acknowledges financial support from the University of Manchester's Dean's Doctoral Scholarship. S.A. acknowledges the support of the Deanship of Scientific Research at Northern Border University, Arar, KSA for funding through the project number NBU-SA-FIR-2025, J.G.M. is supported by the University of Manchester Dame Kathleen Ollerenshaw Fellowship. The authors acknowledge the use of resources provided by the Isambard 3 Tier-2 HPC Facility, hosted by the University of Bristol and operated by the GW4 Alliance (<https://gw4.ac.uk>) and funded by UK Research and Innovation; and the Engineering and Physical Sciences Research Council [EP/X039137/1]; and the Sulis Tier 2 HPC plat-

form hosted by the Scientific Computing Research Technology Platform at the University of Warwick, funded by EPSRC Grant EP/T022108/1 and the HPC Midlands+ consortium.

VII. CONTRIBUTIONS

This was conceived by VF, IR, and KE. Experimental data were obtained and analysed by MM, RP, TI, and KE. IR and VF modelled exchange SOS enhancement. DFT modelling and its tuning was performed by XL and SA. The DFT+U+V model was set by JM and VF and realised by XL and JM. The paper has been written by IR, JM, MM and VF with contributions from all authors.

[1] B. Radisavljevic and A. Kis, Mobility engineering and a metal-insulator transition in monolayer mos₂, *Nature Materials* **12**, 815 (2013).

[2] D. Lembke, S. Bertolazzi, and A. Kis, Single-layer mos₂ electronics, *Accounts of Chemical Research* **48**, 100 (2015).

[3] D. Dumcenco, D. Ovchinnikov, K. Marinov, O. Lopez-Sanchez, D. Krasnozhon, M.-W. Chen, P. Gillet, A. F. i Morral, A. Radenovic, and A. Kis, Large-area epitaxial monolayer mos₂, *ACS Nano* **9**, 4611 (2015).

[4] F. Withers, O. Del Pozo-Zamudio, A. Mishchenko, A. P. Rooney, A. Gholinia, K. Watanabe, T. Taniguchi, S. J. Haigh, A. K. Geim, A. I. Tartakovskii, and K. S. Novoselov, Light-emitting diodes by band-structure engineering in van der waals heterostructures, *Nature Materials* **14**, 301 (2015).

[5] F. Withers, O. Del Pozo-Zamudio, S. Schwarz, S. Dufferwiel, P. M. Walker, T. Godde, A. P. Rooney, A. Gholinia, C. R. Woods, P. Blake, S. J. Haigh, K. Watanabe, T. Taniguchi, I. L. Aleiner, A. K. Geim, V. I. Fal'ko, A. I. Tartakovskii, and K. S. Novoselov, Wse₂ light-emitting tunneling transistors with enhanced brightness at room temperature, *Nano Letters* **15**, 8223 (2015).

[6] Y. Tang, K. F. Mak, and J. Shan, Long valley lifetime of dark excitons in single-layer WSe₂, *Nature Communications* **10**, 4047 (2019).

[7] P. Dey, L. Yang, C. Robert, G. Wang, B. Urbaszek, X. Marie, and S. A. Crooker, Gate-Controlled Spin-Valley Locking of Resident Carriers in WSe₂ Monolayers, *Phys. Rev. Lett.* **119**, 137401 (2017).

[8] D. T. Perkins and A. Ferreira, Spintronics in 2d graphene-based van der waals heterostructures, in *Encyclopedia of Condensed Matter Physics (Second Edition)*, edited by T. Chakraborty (Academic Press, Oxford, 2024) second edition ed., pp. 205–222.

[9] E. C. Ahn, 2d materials for spintronic devices, *npj 2D Materials and Applications* **4**, 17 (2020).

[10] S. Manzeli, D. Ovchinnikov, D. Pasquier, O. V. Yazyev, and A. Kis, 2d transition metal dichalcogenides, *Nature Reviews Materials* **2**, 17033 (2017).

[11] E. C. Regan, D. Wang, E. Y. Paik, Y. Zeng, L. Zhang, J. Zhu, A. H. MacDonald, H. Deng, and F. Wang, Emerging exciton physics in transition metal dichalcogenide heterobilayers, *Nature Reviews Materials* **7**, 778 (2022).

[12] G. Wang, A. Chernikov, M. M. Glazov, T. F. Heinz, X. Marie, T. Amand, and B. Urbaszek, Colloquium: Excitons in atomically thin transition metal dichalcogenides, *Rev. Mod. Phys.* **90**, 021001 (2018).

[13] K. P. O'Brien, C. H. Naylor, C. Dorow, K. Maxey, A. V. Penumatcha, A. Vyatskikh, T. Zhong, A. Kitamura, S. Lee, C. Rogan, W. Mortelmans, M. S. Kavrik, R. Steinhardt, P. Buragohain, S. Dutta, T. Tronic, S. Clendenning, P. Fischer, E. S. Putna, M. Radosavljevic, M. Metz, and U. Avci, Process integration and future outlook of 2d transistors, *Nature Communications* **14**, 6400 (2023).

[14] J. R. Schaibley, H. Yu, G. Clark, P. Rivera, J. S. Ross, K. L. Seyler, W. Yao, and X. Xu, Valleytronics in 2d materials, *Nature Reviews Materials* **1**, 16055 (2016).

[15] P. Yang, F. Liu, X. Li, J. Hu, F. Zhou, L. Zhu, Q. Chen, P. Gao, and Y. Zhang, Highly reproducible epitaxial growth of wafer-scale single-crystal monolayer MoS₂ on sapphire, *Small Methods* **7**, e2300165 (2023).

[16] Y. Xia, X. Chen, J. Wei, S. Wang, S. Chen, P. Zhou, *et al.*, 12-inch growth of uniform MoS₂ monolayer for integrated circuit manufacture, *Nature Materials* **22**, 1324 (2023).

[17] L. Li, Q. Wang, F. Wu, Q. Xu, J. Tian, Z. Huang, Q. Wang, X. Zhao, Q. Zhang, Q. Fan, *et al.*, Epitaxy of wafer-scale single-crystal MoS₂ monolayer via buffer layer control, *Nature Communications* **15**, 1825 (2024).

[18] H. Yu, L. Huang, L. Zhou, Y. Peng, X. Li, P. Yin, J. Zhao, M. Zhu, S. Wang, J. Liu, *et al.*, Eight in. wafer-scale epitaxial monolayer MoS₂, *Advanced Materials* **36**, e2402855 (2024).

[19] J. Kwon, M. Seol, J. Yoo, H. Ryu, D. S. Ko, M. H. Lee, E. K. Lee, M. S. Yoo, G. H. Lee, H. J. Shin, J. Kim, and K. E. Byun, 200-mm-wafer-scale integration of polycrystalline molybdenum disulfide transistors, *Nature Electronics* **7**, 356 (2024).

[20] K. Kang, S. Xie, L. Huang, Y. Han, P. Y. Huang, K. F. Mak, C.-J. Kim, D. A. Muller, and J. Park, High-mobility three-atom-thick semiconducting films with wafer-scale homogeneity, *Nature* **520**, 656 (2015).

[21] N. Aspiotis, K. Morgan, B. März, K. Müller-Caspary, M. Ebert, E. Weatherby, M. E. Light, C.-C. Huang, D. W. Hewak, S. Majumdar, and I. Zeimpekis, Large-area synthesis of high electrical performance mos₂ by a commercially scalable atomic layer deposition process, npj 2D Materials and Applications **7**, 18 (2023).

[22] S. Haastrup, M. Strange, M. Pandey, T. Deilmann, P. S. Schmidt, N. F. Hinsche, M. N. Gjerding, D. Torelli, P. M. Larsen, A. C. Riis-Jensen, J. Gath, K. W. Jacobsen, J. J. Mortensen, T. Olsen, and K. S. Thygesen, The computational 2d materials database: High-throughput modeling and discovery of atomically thin crystals, 2D Materials **5**, 042002 (2018).

[23] J. Zhou, L. Shen, M. D. Costa, K. A. Persson, and S. P. Ong, 2dmatpedia, an open computational database of two-dimensional materials from top-down and bottom-up approaches, Scientific Data **6**, 86 (2019).

[24] D. Campi, N. Mounet, M. Gibertini, G. Pizzi, and N. Marzari, Expansion of the materials cloud 2d database, ACS Nano **17**, 11268 (2023).

[25] N. Mounet, M. Gibertini, P. Schwaller, D. Campi, A. Merkys, A. Marrazzo, T. Sohier, I. E. Castelli, A. Cepellotti, G. Pizzi, and N. Marzari, Two-dimensional materials from high-throughput computational exfoliation of experimentally known compounds, Nature Nanotechnology **13**, 246 (2018).

[26] K. Choudhary, K. F. Garrity, A. C. E. Reid, B. DeCost, A. J. Biacchi, A. R. Hight Walker, Z. Trautt, J. Hattrick-Simpers, A. G. Kusne, A. Centrone, A. Davydov, J. Jiang, R. Pachter, G. Cheon, E. Reed, A. Agrawal, X. Qian, V. Sharma, S. V. Kalinin, B. G. Sumpter, G. Pilania, P. Acar, S. Mandal, K. Haule, D. Vanderbilt, K. Rabe, and F. Tavazza, The joint automated repository for various integrated simulations (jarvis) for data-driven materials design, npj Computational Materials **6**, 173 (2020).

[27] L. Shen, J. Zhou, T. Yang, M. Yang, Y. P. Feng, Y. Zhang, Q. Wang, J. Liu, and J. Wang, High-throughput computational discovery and intelligent design of two-dimensional functional materials for various applications, Accounts of Materials Research **3**, 572 (2022).

[28] B. Lu, Y. Xia, Y. Ren, M. Xie, L. Zhou, G. Vinai, S. A. Morton, A. T. S. Wee, W. G. van der Wiel, W. Zhang, and P. K. J. Wong, When machine learning meets 2d materials: A review, Advanced Science **11**, 2305277 (2024).

[29] A. Kormányos, G. Burkard, M. Gmitra, J. Fabian, V. Zólyomi, N. D. Drummond, and V. Fal'ko, k·p theory for two-dimensional transition metal dichalcogenide semiconductors, 2D Materials **2**, 022001 (2015).

[30] A. Kormányos, V. Zólyomi, N. D. Drummond, P. Rakyta, G. Burkard, and V. I. Fal'ko, Monolayer mos₂: Trigonal warping, the γ valley, and spin-orbit coupling effects, Physical Review B **88**, 045416 (2013).

[31] K. Kośmider, J. W. González, and J. Fernández-Rossier, Large spin splitting in the conduction band of transition metal dichalcogenide monolayers, Phys. Rev. B **88**, 245436 (2013).

[32] T. Cheiwhanchamnangij, W. R. L. Lambrecht, Y. Song, and H. Dery, Strain effects on the spin-orbit-induced band structure splittings in monolayer mos₂ and graphene, Physical Review B **88**, 155404 (2013).

[33] R. Rodrigues Pela, C. Vona, S. Lubeck, B. Alex, I. Gonzalez Oliva, and C. Draxl, Critical assessment of g0w0 calculations for 2d materials: the example of monolayer mos₂, npj Computational Materials **10**, 77 (2024).

[34] K. Marinov, A. Avsar, K. Watanabe, T. Taniguchi, and A. Kis, Resolving the spin splitting in the conduction band of monolayer MoS₂, Nature Communications **8**, 1938 (2017).

[35] R. Pisoni, A. Kormányos, M. Brooks, Z. Lei, P. Back, M. Eich, H. Overweg, Y. Lee, P. Rickhaus, K. Watanabe, T. Taniguchi, A. Imamoglu, G. Burkard, T. Ihn, and K. Ensslin, Interactions and Magnetotransport through Spin-Valley Coupled Landau Levels in Monolayer MoS₂, Phys. Rev. Lett. **121**, 247701 (2018).

[36] J. Lin, T. Han, B. A. Piot, Z. Wu, S. Xu, G. Long, L. An, P. Cheung, P.-P. Zheng, P. Plochocka, X. Dai, D. K. Maude, F. Zhang, and N. Wang, Determining interaction enhanced valley susceptibility in spin-valley-locked mos₂, Nano Letters **19**, 1736 (2019).

[37] Z. Chi, Z. Wei, G. Zhang, H. Chen, and Y.-X. Weng, Determining Band Splitting and Spin-Flip Dynamics in Monolayer MoS₂, The Journal of Physical Chemistry Letters **14**, 9640 (2023), pMID: 37870497, <https://doi.org/10.1021/acs.jpclett.3c02431>.

[38] C. Robert, B. Han, P. Kapuscinski, A. Delhomme, C. Faugeras, T. Amand, M. R. Molas, M. Bartos, K. Watanabe, T. Taniguchi, B. Urbaszek, M. Potemski, and X. Marie, Measurement of the spin-forbidden dark excitons in MoS₂ and MoSe₂ monolayers, Nature Communications **11**, 4037 (2020).

[39] I. Rozhansky and V. Fal'ko, Exchange-enhanced spin-orbit splitting and its density dependence for electrons in monolayer transition metal dichalcogenides, Phys. Rev. B **110**, L161404 (2024).

[40] B. Scharf, D. V. Tuan, I. Žutić, and H. Dery, Dynamical screening in monolayer transition-metal dichalcogenides and its manifestations in the exciton spectrum, Journal of Physics: Condensed Matter **31**, 203001 (2019).

[41] H. Ochoa, F. Finocchiaro, F. Guinea, and V. I. Fal'ko, Spin-valley relaxation and quantum transport regimes in two-dimensional transition-metal dichalcogenides, Phys. Rev. B **90**, 235429 (2014).

[42] URL will be inserted by publisher.

[43] T. Eknaphakul, P. D. C. King, M. Asakawa, P. Buaphet, R.-H. He, S.-K. Mo, H. Takagi, K. M. Shen, F. Baumberger, T. Sasagawa, S. Junghawan, and W. Meevasana, Electronic structure of a quasi-free-standing mos₂ monolayer, Nano Letters **14**, 1312 (2014).

[44] G. Giuliani and G. Vignale, *Quantum Theory of the Electron Liquid* (Cambridge University Press, 2005).

[45] S. Das Sarma, V. M. Galitski, and Y. Zhang, Temperature-dependent effective-mass renormalization in two-dimensional electron systems, Phys. Rev. B **69**, 125334 (2004).

[46] Y. Zhang and S. Das Sarma, Temperature-dependent effective mass renormalization in a coulomb fermi liquid, Phys. Rev. B **70**, 035104 (2004).

[47] V. M. Galitski and S. Das Sarma, Universal temperature corrections to fermi liquid theory in an interacting electron system, Phys. Rev. B **70**, 035111 (2004).

[48] A. Galiautdinov, Anisotropic keldysh interaction, Physics Letters A **383**, 3167 (2019).

[49] A. Ceferino, K. W. Song, S. J. Magorrian, V. Zólyomi, and V. I. Fal'ko, Crossover from weakly indirect to direct excitons in atomically thin films of inse, Phys. Rev. B **101**, 245432 (2020).

[50] A. Pierret, D. Mele, H. Graef, J. Palomo, T. Taniguchi, K. Watanabe, Y. Li, B. Tourny, C. Journet, P. Steyer, V. Garnier, A. Loiseau, J.-M. Berroir, E. Bocquillon, G. Fève, C. Voisin, E. Baudin, M. Rosticher, and B. Plaçais, Dielectric permittivity, conductivity and breakdown field of hexagonal boron nitride, *Materials Research Express* **9**, 065901 (2022).

[51] I. Kylänpää and H.-P. Komsa, Binding energies of exciton complexes in transition metal dichalcogenide monolayers and effect of dielectric environment, *Phys. Rev. B* **92**, 205418 (2015).

[52] E. Menéndez-Proupin, E. S. Morell, G. E. Marques, and C. Trallero-Giner, Lattice vibration modes and electron-phonon interactions in monolayer vs. bilayer of transition metal dichalcogenides, *RSC Advances* **14**, 5234 (2024).

[53] S. Das Sarma and E. H. Hwang, Screening and transport in 2d semiconductor systems at low temperatures, *Scientific Reports* **5**, 16655 (2015).

[54] A. V. Chubukov and D. L. Maslov, Nonanalytic corrections to the fermi-liquid behavior, *Phys. Rev. B* **68**, 155113 (2003).

[55] A. Principi, G. Vignale, M. Carrega, and M. Polini, Intrinsic lifetime of dirac plasmons in graphene, *Phys. Rev. B* **88**, 195405 (2013).

[56] A. V. Chubukov and D. L. Maslov, Universal and nonuniversal renormalizations in fermi liquids, *Phys. Rev. B* **81**, 245102 (2010).

[57] Y. Gindikin and A. V. Chubukov, Fermi surface geometry and optical conductivity of a two-dimensional electron gas near an ising-nematic quantum critical point, *Phys. Rev. B* **109**, 115156 (2024).

[58] T. Ando, A. B. Fowler, and F. Stern, Electronic properties of two-dimensional systems, *Rev. Mod. Phys.* **54**, 437 (1982).

[59] S. Azadi, N. D. Drummond, A. Principi, R. V. Belosudov, and M. S. Bahramy, Quantum monte carlo study of the quasiparticle effective mass of the two-dimensional uniform electron liquid, *Phys. Rev. B* **112**, 075141 (2025).

[60] J. P. Echeverry, B. Urbaszek, T. Amand, X. Marie, and I. C. Gerber, Splitting between bright and dark excitons in transition metal dichalcogenide monolayers, *Phys. Rev. B* **93**, 121107 (2016).

[61] M. N. Gjerding, A. Taghizadeh, A. Rasmussen, S. Ali, F. Bertoldo, T. Deilmann, N. R. Knøsgaard, M. Kruse, A. H. Larsen, S. Manti, T. G. Pedersen, U. Petralanda, T. Skovhus, M. K. Svendsen, J. J. Mortensen, T. Olsen, and K. S. Thygesen, Recent progress of the computational 2d materials database (c2db), *2D Materials* **8**, 044002 (2021).

[62] This value can be compared with optical data on hBN-encapsulated MoS₂ monolayers [38]. Unlike magnetotransport, where many-body interactions renormalize effective masses and SOS, optical spectroscopy probes excitons without free carriers and thus reflects nearly unrenormalized single-particle parameters. Using the framework of Ref. [78] and the code of Ref. [79], we recalculate the bare Δ_0 needed to reproduce the reported bright-dark exciton splitting $\Delta_{BD} = 14$ meV [38], which depends on

$$\Delta_{BD} = -\Delta_0 + \Delta_{\text{bind}} + \Delta_{\text{exch}}, \quad (6)$$

Taking $m_h \approx 0.6m_e$ [43], we obtain $\Delta_{\text{bind}} \approx 19.5$ meV and $\Delta_{\text{exch}} \approx 2.6$ meV.

[63] G.-B. Liu, D. Xiao, Y. Yao, X. Xu, and W. Yao, Electronic structures and theoretical modelling of two-dimensional group-vib transition metal dichalcogenides, *Chem. Soc. Rev.* **44**, 2643 (2015).

[64] R. Pisoni, T. Davatz, K. Watanabe, T. Taniguchi, T. Ihn, and K. Ensslin, Absence of interlayer tunnel coupling of k -valley electrons in bilayer mos₂, *Phys. Rev. Lett.* **123**, 117702 (2019).

[65] M. Masseroni, T. Qu, T. Taniguchi, K. Watanabe, T. Ihn, and K. Ensslin, Evidence of the coulomb gap in the density of states of mos₂, *Phys. Rev. Res.* **5**, 013113 (2023).

[66] M. Masseroni, T. Davatz, R. Pisoni, F. K. de Vries, P. Rickhaus, T. Taniguchi, K. Watanabe, V. Fal'ko, T. Ihn, and K. Ensslin, Electron transport in dual-gated three-layer Mos₂, *Phys. Rev. Res.* **3**, 023047 (2021).

[67] M. Masseroni, *Electronic transport experiments in 2D materials with spin-orbit coupling*, Ph.D. thesis, ETH Zurich (2024).

[68] M. Masseroni, I. Soltero, J. G. McHugh, I. Rozhansky, X. Li, A. Schmidhuber, M. Niese, T. Taniguchi, K. Watanabe, V. I. Fal'ko, T. Ihn, and K. Ensslin, Gate-tunable band edge in few-layer mos₂, *Nano Letters* **25**, 10472 (2025).

[69] V. L. Campo and M. Cococcioni, Extended dft+ u+ v method with on-site and inter-site electronic interactions, *Journal of Physics: Condensed Matter* **22**, 055602 (2010).

[70] K. F. Mak, K. He, J. Shan, and T. F. Heinz, Control of valley polarization in monolayer MoS₂ by optical helicity, *Nature Nanotechnology* **7**, 494 (2012).

[71] A. R. Klots, A. K. M. Newaz, B. Wang, D. Prasai, H. Krzyzanowska, J. Lin, D. Caudel, N. J. Ghimire, J. Yan, B. L. Ivanov, K. A. Velizhanin, A. Burger, D. G. Mandrus, N. H. Tolk, S. T. Pantelides, and K. I. Bolotin, Probing excitonic states in suspended two-dimensional semiconductors by photocurrent spectroscopy, *Scientific Reports* **4**, 6608 (2014).

[72] W. Li, A. G. Birdwell, M. Amani, R. A. Burke, X. Ling, Y.-H. Lee, X. Liang, L. Peng, C. A. Richter, J. Kong, D. J. Gundlach, and N. V. Nguyen, Broadband optical properties of large-area monolayer cvd molybdenum disulfide, *Phys. Rev. B* **90**, 195434 (2014).

[73] D. Kozawa, R. Kumar, A. Carvalho, K. Kumar Amara, W. Zhao, S. Wang, M. Toh, R. M. Ribeiro, A. H. Castro Neto, K. Matsuda, and G. Eda, Photocarrier relaxation pathway in two-dimensional semiconducting transition metal dichalcogenides, *Nature Communications* **5**, 4543 (2014).

[74] J. P. Perdew and M. Levy, Physical content of the exact kohn-sham orbital energies: Band gaps and derivative discontinuities, *Phys. Rev. Lett.* **51**, 1884 (1983).

[75] A. Sampanraj, L. Devendar, B. Pothal, M. Jaiswal, and J. Balakrishnan, Interface-controlled thermal transport in monolayer molybdenum disulfide, *Phys. Rev. B* **111**, 075423 (2025).

[76] K. F. Mak, C. Lee, J. Hone, J. Shan, and T. F. Heinz, Atomically thin mos₂: A new direct-gap semiconductor, *Phys. Rev. Lett.* **105**, 136805 (2010).

[77] H. R. Ramezani, E. Şaşioğlu, H. Hadipour, H. R. Soleimani, C. Friedrich, S. Blügel, and I. Mertig, Nonconventional screening of coulomb interaction in two-dimensional semiconductors and metals: A comprehensive constrained random phase approximation study of

with Δ_{bind} determined by the effective masses m_l , m_u , and m_h , and Δ_{exch} the short-range exciton exchange.

mX_2 ($m = \text{Mo, W, Nb, Ta}; x = \text{S, Se, Te}$), Phys. Rev. B **109**, 125108 (2024).

[78] M. Szyniszewski, E. Mostaani, N. D. Drummond, and V. I. Fal'ko, Binding energies of trions and biexcitons in two-dimensional semiconductors from diffusion quantum monte carlo calculations, Phys. Rev. B **95**, 081301 (2017).

[79] E. Mostaani, M. Szyniszewski, C. H. Price, R. Maezono, M. Danovich, R. J. Hunt, N. D. Drummond, and V. I. Fal'ko, Diffusion quantum monte carlo study of excitonic complexes in two-dimensional transition-metal dichalcogenides, Phys. Rev. B **96**, 075431 (2017).